SUPPORTING INFORMATION

High Gradient Nanomagnets on Cantilevers for Sensitive Detection of Nuclear Magnetic Resonance

Jonilyn G. Longenecker,[1] H. J. Mamin,[2] Alexander W. Senko,[3] Lei Chen,[1] Charles T. Rettner,[2] Daniel Rugar,[2] and John A. Marohn[1,*]

[1]*Department of Chemistry and Chemical Biology, Cornell University, Ithaca, New York 14853*

[2]*IBM Research Division, Almaden Research Center, San Jose, California 95120*

[3]*Department of Materials Science and Engineering, Cornell University, Ithaca, New York 14853*

(Dated: September 28, 2012)

In this supplement we describe the improved focused ion beam (FIB) liftout procedure used to assemble the magnet-tipped chip on the cantilever, present an X-ray photoelectron spectroscopy (XPS) study of the extent of oxidation damage to the magnet, and report the saturation magnetization for a large-area cobalt magnetic thin film studied by superconducting quantum interference device (SQUID) magnetometry as a control for the magnetization of the nanomagnet studied in the manuscript. Additionally, details of the simulations carried out to study tip performance, an experimental study of the power spectral density of the cantilever frequency fluctuations, and a discussion of the highest-sensitivity scanned probe magnetic resonance measurements to-date are presented.

Magnet chip additional details. Two key changes have been made to the design of the magnet-tipped chips in order to improve the process of attaching them to our custom attonewton-sensitivity cantilevers since publication of the original procedure [1]. Scanning electron microscope (SEM) images of the FIB liftout and attachment procedure used here are shown in Fig. S1. In this revised protocol, a side tab has been added to the chip design (Fig. S1(a)). This side tab eliminated the risk of milling into the cantilever when the probe needle was milled and removed from the chip-on-cantilever assembly at the end of the process. Additionally, modifications were made to the chip body in order to further refine its shape in preparation for adhesion to the cantilever (Fig. S1(b)). These improvements to the chip shape, specifically the addition of two rectangular holes on the chip side and a tapered back edge, provided increased surface area for the platinum welds to adhere the chip to the cantilever during attachment (Fig. S1(c-e)).

XPS sample preparation. A CVC SC4500 E-gun Evaporation System was used to blanket-deposit titanium (4 nm) adhesion layers and cobalt (81 nm) thin films on silicon wafers. The nanomagnet studied in the manuscript was capped with 8 nm of platinum on the top of the magnet, but the leading edge (sidewall) of the magnet was unprotected. In order to understand the damage at this nanomagnet sidewall, blanket-deposited cobalt thin films were prepared without a capping layer (Fig. S2). To assess the damage to the top and center of the nanomagnet, other films were prepared with an 8 nm platinum capping layer (Fig. S3). One capped and one uncapped sample were exposed to air for one week and studied with no post-deposition processing to determine the inherent oxidation damage; these are labeled in Fig. S2 and S3 as the 'unbaked' samples. A second set of samples were exposed to air for the same period of time, but they were spin-coated with 2 μm of 495,000 molecular weight (poly)methylmethacrylate (PMMA) resist and baked at 115°C for 40 minutes prior to analysis in order to emulate the processing conditions of the nanomagnet; these are labeled as the 'baked' films in the figures. Note that the relative thicknesses were measured *in situ* with a quartz crystal microbalance and the total film thickness of a test sample was measured by atomic force microscope (AFM) profilometry.

XPS methods. Samples were analyzed by XPS using a Surface Science Instruments model SSX-100 spectrometer with monochromated aluminum K_α X-rays (1486.6 eV) and a beam diameter of 1 mm. Photoemitted electrons were collected at a 55 degree emission angle using a hemispherical analyzer with a 150 V pass energy. Depth profiling was performed using an argon ion source with an ion energy of 500 eV (Fig. S2), 1000 eV (Fig. S3(baked)), or 4000 eV (all other samples); the total beam current was 1 μA and the ion beam was rastered over a 1.5×2.5 mm area. Survey scans over 0-1000 eV were used to determine atomic composition *versus* depth using the following peaks: Co 2p, Pt 4f (Fig. S3) or Pt 4d (Fig. S4), O 1s, Ti 2p, and Si 2s. The spectroscopic data were used to calculate atomic percent composition of the film by using the Shirley background and integrating under the appropriate peaks. The count rates for the representative peaks of each element present were scaled by their relative sensitivity factors to calculate the atomic percent composition for each spectrum.

Estimation of sample composition as a function of depth, as shown in Figs. S2 to S4, was enabled by measuring the total etch depth of each ion-milled recess *ex situ* by stylus profilometry and linearly converting from etch time to etch depth. To confirm that a linear conversion was appropriate, the film in Fig. S4 was etched through to the silicon substrate. For comparison, the relative thicknesses of the layers

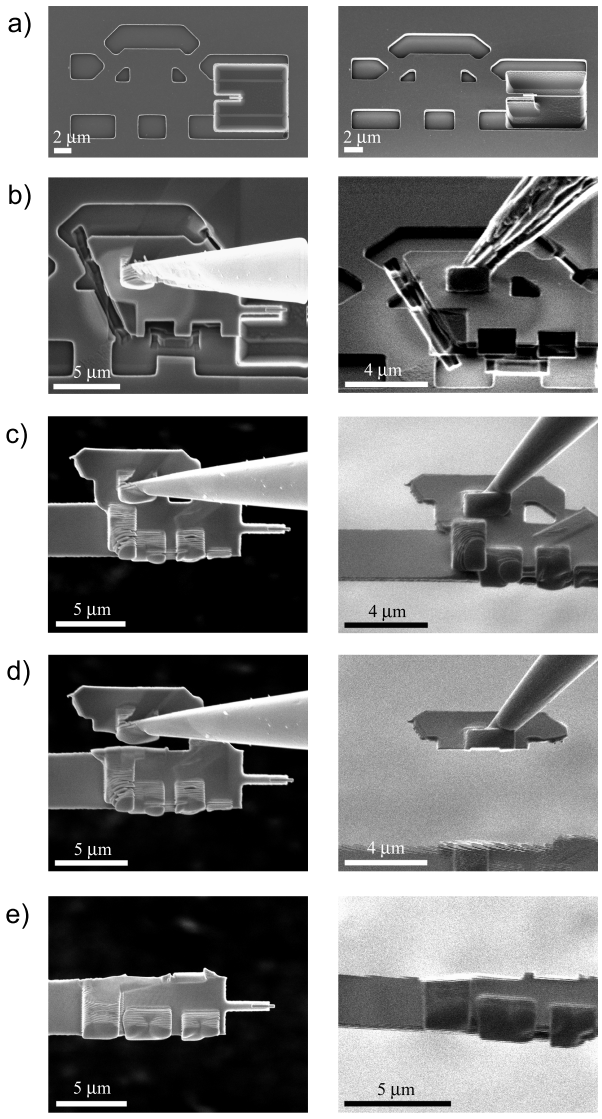

FIG. S1: FIB attachment procedure. Top-down (SEM) and side-on (FIB) images of the key steps used to remove the magnet-tipped silicon chip from the substrate [panels (a)-(b)] and attach it to the leading edge of a blank cantilever [panels (c)-(e)]. To remove the chip from the substrate, a probe needle was attached to the silicon tab connected to the chip, the support tabs were milled, and the shape of the chip was fine-tuned in order to promote superior adhesion to the cantilever by milling rectangular holes into the side of the chip and angling the back edge of the chip [panel (b)]. The chip was positioned over the leading edge of the cantilever and adhered to the cantilever by depositing FIB-assisted platinum in the rectangular holes and at the back edge of the chip [panel (c)]. The tab at the side of the chip was milled away [panel (d)] in order to cleanly separate the probe tip from the chip-cantilever assembly [panel (e)].

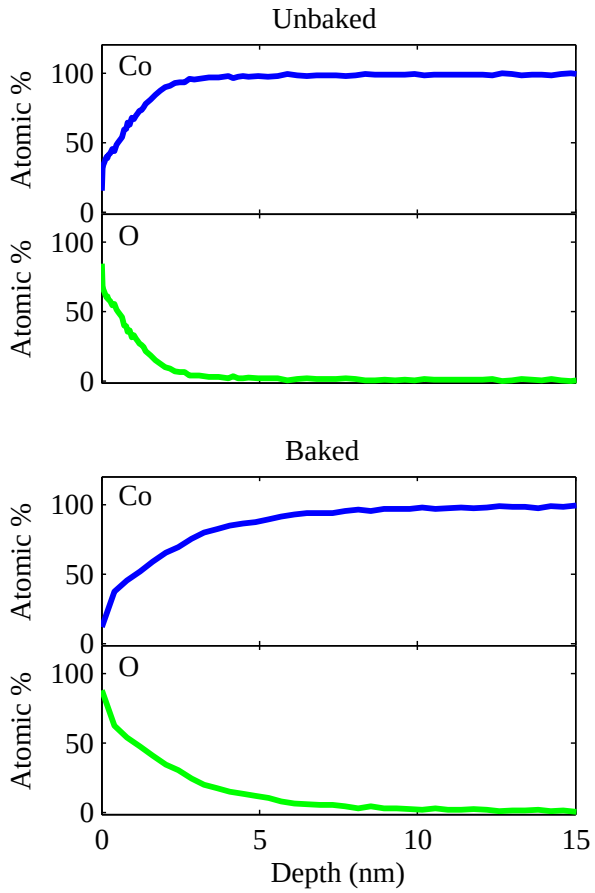

FIG. S2: XPS depth profiles of unbaked and baked blanket-deposited cobalt films. Atomic concentrations as a function of depth are shown for cobalt (blue) and oxygen (green). The two films are from portions of the same wafer; both films were exposed to ambient conditions for one week prior to analysis, and one film was coated with PMMA resist and baked at 115°C for 40 minutes in order to simulate processing damage to the leading edge of the nanomagnet studied in the manuscript. When compared to the unbaked TiCo sample (upper), oxygen was observed 3 to 5 nm deeper into the baked TiCo film (lower), indicating that heat exposure induced 3-5 nm of additional surface oxidation.

were measured by an *in situ* quartz crystal microbalance during deposition and the total film thickness was measured after deposition by AFM profilometry. The layer thicknesses were determined by AFM to be 4.1 ± 0.05 nm of titanium, 81.4 ± 1.0 nm of cobalt, and 8.1 ± 0.1 nm of platinum. These thicknesses agreed well with the depths calculated using XPS depth profiling with linear conversion from milling time to depth. Since the same process was used to convert all etch times to depth, the depth profiles for the films in Figs. S2 and S3 should thus also be accurate. The etch time-to-depth conversion factors and the intervals between points for each film were 0.31 nm/min and 0.17 nm/point for Fig. S2(unbaked), 0.81 nm/min and 0.33 nm/point for Fig. S2(baked), 6.6 nm/min and 1.7 nm/point for Fig. S3(unbaked), 1.0 nm/min and 0.25 nm/point for Fig. S3(baked), and 1.8 nm/min and 9.0 nm/point for Fig. S4.

SQUID magnetometry methods. To independently confirm the cobalt magnetization, a circular bulk thin-film cobalt sample was studied using SQUID magnetometry (Fig. S5). A circle of radius 850 µm was patterned on a 500 µm-thick

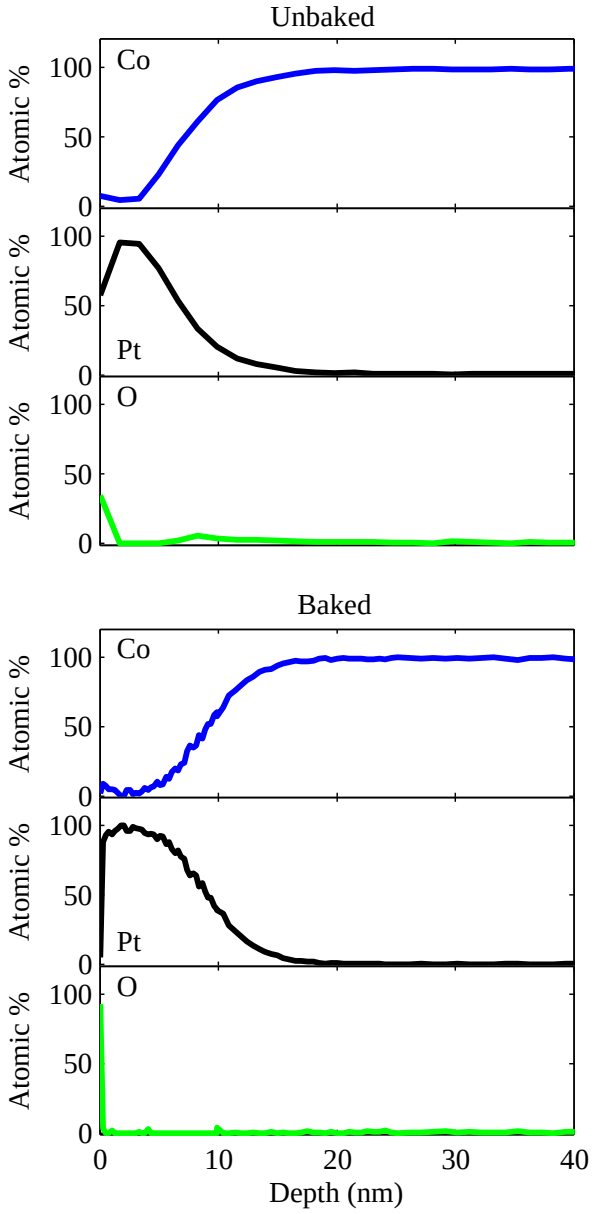

FIG. S3: XPS depth profiles of unbaked and baked blanket-deposited cobalt films that were capped with 8 nm of platinum to mitigate surface oxidation. Atomic concentrations as a function of depth are shown for cobalt (blue), platinum (black), and oxygen (green). The two films are from portions of the same wafer; both films were exposed to air for one week prior to analysis, and the baked film was coated with PMMA resist and baked at 115°C for 40 minutes. No oxygen was observed in the cobalt layer of either film, which indicates that platinum capping successfully inhibited oxidation.

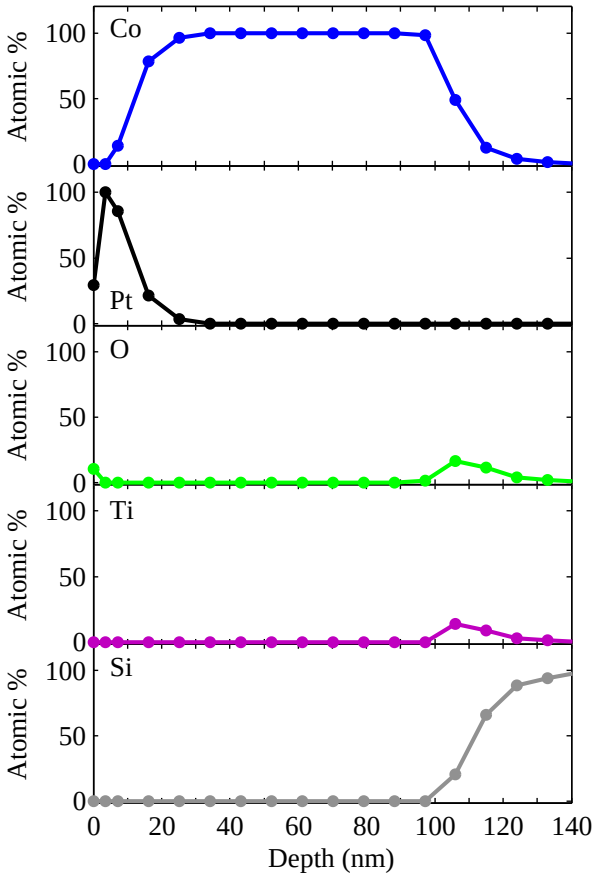

FIG. S4: A cobalt film was evaporated onto a silicon substrate using a titanium adhesion layer and a platinum capping layer to protect against oxidation. The XPS depth profile details the atomic concentrations of cobalt (blue), platinum (black), oxygen (green), titanium (purple), and silicon (gray) as a function of depth in the film at approximately 9 nm/point spacing (data points indicated by filled circles). The depth at each point was measured as a linear conversion from the percentage of the total time etched multiplied by the total etch depth that was measured by profilometry. The thicknesses measured by XPS can be compared to the thicknesses measured by the AFM-based approach discussed in the Supporting Information XPS methods section to determine the validity of this linear conversion from etch time to depth; the thicknesses of the layers measured by the AFM-based approach are titanium (4.1 $\pm$ 0.05 nm), cobalt (81.4 $\pm$ 1.0 nm), and platinum (8.1 $\pm$ 0.1 nm), which roughly agree with the XPS thicknesses.

fused silica wafer using contact photolithography and liftoff. Employing the same procedure used to deposit the nanomagnet, a film of titanium (4.2 nm), cobalt (84.3 nm), and platinum (8.4 nm) was deposited. The wafer was diced into 6.5 $\times$ 6.5 mm pieces using a KS 7100 Dicing Saw. After dicing, the resulting chips were handled with plastic tweezers to minimize ferromagnetic contamination. SQUID magnetometry was conducted using a Quantum Design MPMS-XL SQUID Magnetometer. The chip was centered in a plastic drinking straw sample holder that had a diameter such that the sample fit snugly inside. The drinking straw was adhered to the end of a sample rod using Kapton tape, the sample was inserted into the magnetometer, and the system was stabilized at 4.0 K for 30 minutes. Prior to data collection the field was ramped to +3.0 T in steps of 0.5 T. Data was collected between +3 T and -3 T, first sweeping positive to negative fields and then negative to positive, using the following field step sizes:

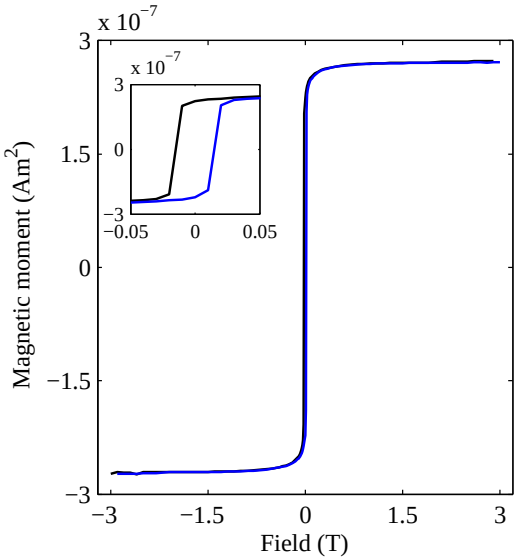

FIG. S5: In-plane magnetization loop obtained at 4.0 K using SQUID magnetometry. The magnetic film was deposited using the same process as for the nanomagnet shown in the manuscript in Fig. 2(b); the thin film consisted of 4.2 nm of titanium, 84.3 nm of cobalt, and 8.4 nm of platinum. The sample was a circle with a radius of 850 μm supported on a 6.5×6.5 mm^2 fused silica substrate. The magnetization was swept from $+3$ T to -3 T (black) and then from -3 T to $+3$ T (blue). For this magnetization and magnetic volume, the data corresponds to a saturation magnetization of $\mu_0 M_{\rm sat} = 1.8 \pm 0.1$ T.

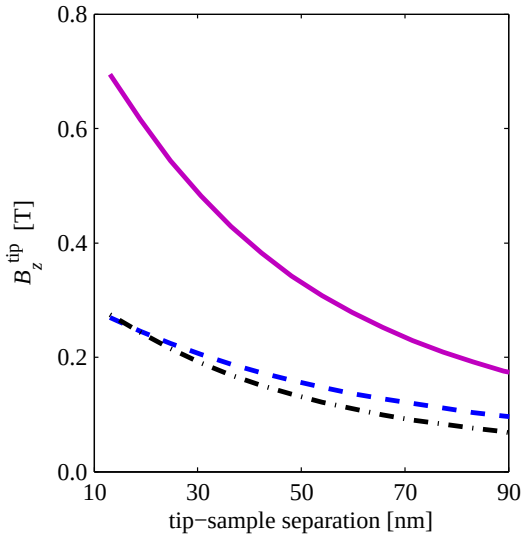

FIG. S6: Comparison of numerical simulations of the tip fields produced by the damage model plotted in the manuscript in Fig. 5 in which the magnet had 51 nm of damage at the leading edge (Method 1; blue dashed line) to (1) a completely intact magnetic particle with a magnetization of 1.8 T (purple solid line) and (2) a magnet with a uniformly reduced magnetization of 0.69 T (Method 2; black dot-dashed line).

0.01 T between fields of 0.00 T and ±0.15 T, 0.05 T between fields of ±0.15 T and ±0.50 T, and 0.1 T between fields of ±0.50 T and ±3.0 T.

SQUID magnetometry results. Representative SQUID magnetometry data is shown in Fig. S5. The magnetic moment of the film was calculated by subtracting the linear diamagnetic background of the fused silica chip from the total signal. To convert to saturation magnetization, the magnetic moment was averaged in the saturated regime and was divided by the volume of the thin film sample. The film diameter was measured by optical microscopy and the cobalt thickness was determined by using an *in situ* quartz crystal microbalance and conducting AFM profilometry on the sample edge. The data of Fig. S5 indicates a saturation magnetization for the bulk cobalt thin film of $\mu_0 M_{\rm sat} = 1.8 \pm 0.1$ T, which agrees well with the expected value of $\mu_0 M_{\rm sat} = 1.8$ T.

Model calculations for MRFM signal. The model curves appearing in the manuscript in Fig. 4 and in the Supporting Information in Fig. S6 are based on numerical calculations of the MRFM signal as a function of rf center frequency $f_{\rm rf}$ for various tip-sample separations. Since the sample spins are unpolarized, the MRFM signal has time-varying amplitude and sign. To accommodate the statistical nature of the signal, we measured the variance of the ac force generated while the spins underwent cyclic inversion. As discussed in the manuscript and supporting information in Ref. 2, the force variance can be calculated from the three-dimensional convolution integral

$$\sigma^2_{\rm spin}(\mathbf{r}_s) = \int_{\substack{\rm sample \\ \rm volume}} {\rm d}^3(\mathbf{r})\, K(\mathbf{r}_s - \mathbf{r})\rho(\mathbf{r}), \qquad \text{(S1)}$$

where $\sigma^2_{\rm spin}(\mathbf{r}_s)$ is the signal (force variance) as a function of the tip scan position $\mathbf{r}_s$, $K(\mathbf{r})$ is the point spread function associated with the resonant slice, and $\rho(\mathbf{r})$ is the proton number density of the sample. The sample used in the experiment was approximated as a 40 nm thick slab of polystyrene with $\rho(\mathbf{r})$ assumed to be 4.9×10^{28} protons/m^3 within the slab, and zero outside.

The point spread function $K(\mathbf{r})$ is defined to be the force variance generated by a randomly polarized proton spin at a position $\mathbf{r}$ with respect to the magnetic tip. $K(\mathbf{r})$ depends on a number of factors, including the total polarizing field $B_0(\mathbf{r})$ and lateral field gradient $G(\mathbf{r}) = \partial B_z^{\rm tip}/\partial x$:

$$K(\mathbf{r}) = A{\mu_p}^2 [G(\mathbf{r})]^2 \eta\left(\Delta B_0(\mathbf{r})\right). \qquad \text{(S2)}$$

Here A is an overall constant, typically close to unity, that depends on the correlation time of the statistical polarization, detection bandwidth, and Fourier component of the cyclic spin inversion; $\mu_p = 1.4 \times 10^{26}$ J/T is the proton magnetic moment; $\eta\left(\Delta B_0(\mathbf{r})\right)$ is a function that characterizes the off-resonance spin response, where $\Delta B_0(\mathbf{r}) = B_0(\mathbf{r}) - 2\pi f_{\rm rf}/\gamma_{\rm p}$. $\gamma_{\rm p}/2\pi = 42.56$ MHz/T is the proton gyromagnetic ratio and $B_0(\mathbf{r}) =$

$|\mathbf{B}^{\text{ext}} + \mathbf{B}^{\text{tip}}(\mathbf{r})|$ is the total polarizing field, which includes both the z-oriented external field $\mathbf{B}^{\text{ext}}$ and the tip field $\mathbf{B}^{\text{tip}}$.

The off-resonance response depends on the details of the cyclic inversion which generates the oscillating force that drives the cantilever. For the present experiment, where triangle-wave frequency modulation with peak-to-peak FM deviation $\Delta f_{\text{FM}} = 2$ MHz was used to cyclically invert the spins, it was found that the off-resonance response is well approximated by

$$\eta\left(\Delta B_0(\mathbf{r})\right) = \begin{cases} \cos^2\left(\dfrac{\gamma_{\text{p}} \Delta B_0(\mathbf{r})}{2\Delta f_{\text{FM}}}\right) & \text{for } \Delta B_0(\mathbf{r}) \leq \pi \Delta f_{\text{FM}}/\gamma_{\text{p}}, \\ 0 & \text{otherwise.} \end{cases} \tag{S3}$$

The tip field $\mathbf{B}^{\text{tip}}$ and tip-field gradient G were calculated assuming that the tip was a uniformly magnetized rectangular cuboid with a magnetic spacing that exceeded the physical tip-sample separation by 51 nm. The magnet was assumed to have the same saturated magnetic moment as bulk cobalt ($\mu_0 M_{\text{sat}} = 1.8$ T). The width (225 nm) and thickness (79 nm) of the nanomagnet were based on the experimentally observed values; the length of the magnet was set by subtracting the extraneous spacing of 51 nm from the experimentally observed length of 1494 nm.

Combining the tip field calculations with eqs S1 to S3 allowed simulation of MRFM signal *versus* rf frequency at various tip-sample separations, as shown by the smooth curves in Fig. 4 in the manuscript. The width of the MRFM response for all the curves in Fig. 4 could be fit using a single value for an extraneous spacing of 51 nm (Method 1 in the manuscript). The heights of the curves were individually adjusted by varying the A parameter in eq S2. Once the extraneous spacing was determined, the tip parameters were used to generate the field and gradient curves in Fig. 5 in the manuscript and Fig. S6. At the closest tip-sample separations of 13.1 nm, the predicted tip-field gradient $\partial B_z^{\text{tip}}/\partial z = 4.4\,\text{MT m}^{-1}$ ($44\,\text{G nm}^{-1}$).

The tip parameters used to fit the data in Fig. 4 are not unique. For example, a fit of similar quality was obtained by setting the extraneous spacing to zero and instead reducing the tip magnetization to $\mu_0 M_{\text{sat}} = 0.69$ T (Method 2 in the manuscript). This resulted in an estimated tip-field gradient of 5.4 MT m^{-1} for a tip-sample separation of 13.1 nm. In Fig. S6, we compare the simulation results from Method 1 and Method 2 to a fully magnetized cobalt nanomagnet. We can see that the fully magnetized tip overestimates the tip field by more than a factor of two.

In addition to the vertical tip-field gradients, we also calculated lateral gradients $\partial B_x/\partial z$ for our nanomagnet using the Method 1 and Method 2 tip models. The gradients are reported in Table I.

Cantilever frequency noise findings. In Fig. S7 we plot the power spectral density of cantilever frequency fluctuations $S_{\delta f_c}(f)$ over both the polystyrene-coated silicon substrate and the polystyrene-coated copper microwire. Below $f \leq 10$ Hz, $S_{\delta f_c} \propto f^{-1}$, indicative of frequency noise arising from dielectric fluctuations coupling to tip charge [3, 4]. At high frequencies, $f \geq 50$ Hz, $S_{\delta f_c} \propto f^2$ as expected due to detector noise [3, 5]. Over the polystyrene-coated silicon substrate, $S_{\delta f_c}$ approaches the thermal limit at intermediate frequencies. Over the polystyrene-coated copper microwire at intermediate frequencies, in contrast, the power spectral density of cantilever frequency fluctuations is up to 10^6 larger than the thermal limit. The discreteness of the $S_{\delta f_c}$ spectrum over the microwire suggests frequency noise arising from coupling to vibrations [6].

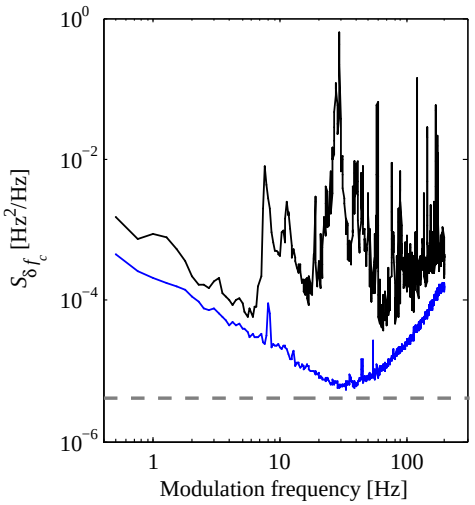

FIG. S7: The power spectral density of the cantilever frequency fluctuations $S_{\delta f_c}$ *versus* modulation frequency was measured over the copper microwire at 2.63 T (upper line, black) and over the silicon substrate at 0 T (lower line, blue). In both cases the surface was coated with 40 nm of polystyrene. The leading edge of the nanomagnet tip was 90 nm from the surface, and the peak-to-peak amplitude was 60 nm. The thermal noise, which was calculated to be 4.0×10^{-6} Hz^2/Hz, is shown as the gray dashed line.

reference	magnet location	magnet material	h [nm]	$\partial B_z^{\rm tip}/\partial z$ [MT m^{-1}]	$\partial B_z^{\rm tip}/\partial x$ [MT m^{-1}]	measurement
Method 1 in this work[a]	on cantilever	Co	13	4.4	2.7	NMR
Method 2 in this work[b]	on cantilever	Co	13	5.4	8.3	NMR
7	on cantilever	$SmCo_5$		0.55	0.43	ESR
8	on cantilever	$SmCo_5$		—	0.2	ESR
9	on cantilever	$SmCo_5$		0.13	—	ESR
10	on cantilever	$SmCo_5$		0.1	—	NMR
11	on cantilever	$SmCo_5$		0.25	—	ESR
12	off cantilever	Dy	21	7.4	4.6	NMR
2	off cantilever	$Fe_{70}Co_{30}$	24	4.2[c]	3.4[c]	NMR

[a] Nanomagnet modeled with an extraneous spacing of 51 nm.
[b] Nanomagnet modeled with a uniformly reduced magnetization of 0.69 T.
[c] Here we report the revised gradient estimate used in Ref. 12.

TABLE I: Vertical ($\partial B_z^{\rm tip}/\partial z$) and lateral ($\partial B_z^{\rm tip}/\partial x$) magnetic field gradients achieved in high sensitivity magnetic resonance force microscope experiments. Tip-sample separation h is listed when available. Note that 1 G nm^{-1} $= 1 \times 10^5$ T m^{-1} $= 0.1$ MT m^{-1}.

Comparison to other high-gradient tips. In Table I, we list the highest reported tip-field gradients to date employed in NMR- and ESR-MRFM measurements. The cobalt nanomagnet studied in the manuscript has both vertical and lateral gradients that are almost an order of magnitude larger than any prior gradient achieved by affixing a magnet to the leading edge of an attonewton-sensitivity cantilever.

* Electronic address: jam99@cornell.edu

[1] Longenecker, J. G.; Moore, E. W.; Marohn, J. A. *J. Vac. Sci. Technol. B* **2011**, *29*, 032001.
[2] Degen, C. L.; Poggio, M.; Mamin, H. J.; Rettner, C. T.; Rugar, D. *Proc. Natl. Acad. Sci. U.S.A.* **2009**, *106*, 1313 – 1317.
[3] Yazdanian, S. M.; Marohn, J. A.; Loring, R. F. *J. Chem. Phys.* **2008**, *128*, 224706.
[4] Yazdanian, S. M.; Hoepker, N.; Kuehn, S.; Loring, R. F.; Marohn, J. A. *Nano Lett.* **2009**, *9*, 2273 – 2279.
[5] Albrecht, T. R.; Grütter, P.; Horne, D.; Rugar, D. *J. Appl. Phys.* **1991**, *69*, 668 – 673.
[6] Hoepker, N.; Lekkala, S.; Loring, R. F.; Marohn, J. A. *J. Phys. Chem. B* **2011**, *115*, 14493 – 14500.
[7] Mamin, H. J.; Budakian, R.; Chui, B. W.; Rugar, D. *Phys. Rev. Lett.* **2003**, *91*, 207604.
[8] Rugar, D.; Budakian, R.; Mamin, H. J.; Chui, B. W. *Nature* **2004**, *430*, 329 – 332.
[9] Fong, K. C.; Herman, M. R.; Banerjee, P.; Pelekhov, D. V.; Hammel, P. C. *Phys. Rev. B* **2011**, *84*, 220405.
[10] Mamin, H. J.; Budakian, R.; Chui, B. W.; Rugar, D. *Phys. Rev. B* **2005**, *72*, 024413.
[11] Bruland, K. J.; Dougherty, W. M.; Garbini, J. L.; Sidles, J. A.; Chao, S. H. *Appl. Phys. Lett.* **1998**, *73*, 3159.
[12] Mamin, H. J.; Rettner, C. T.; Sherwood, M. H.; Gao, L.; Rugar, D. *Appl. Phys. Lett.* **2012**, *100*, 013102.